

# Transport in Mn spinel oxides alloyed with Zn–Ni: Polaron hopping in an inhomogeneous energy landscape

Cite as: J. Appl. Phys. **132**, 115101 (2022); <https://doi.org/10.1063/5.0105553>

Submitted: 24 June 2022 • Accepted: 20 August 2022 • Published Online: 15 September 2022

 Dimitra Katerinopoulou,  Emmanouil Pervolarakis,  Charalampos Papakonstantinou, et al.



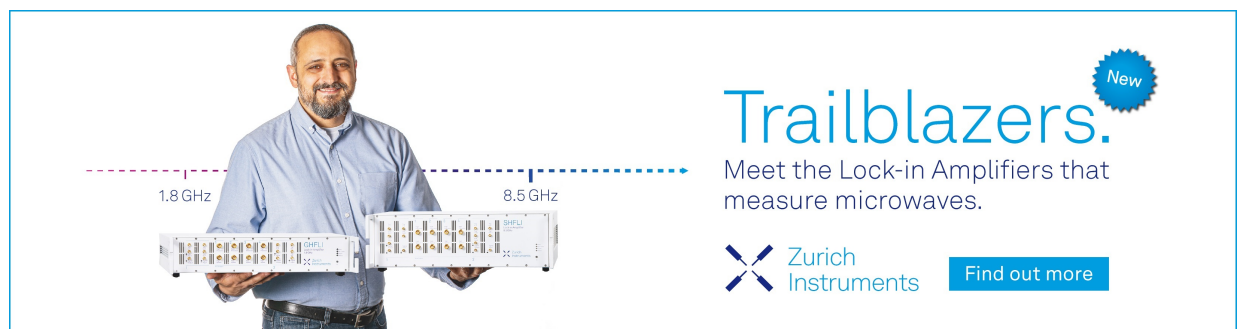
View Online




Export Citation




CrossMark



**Trailblazers.** 

Meet the Lock-in Amplifiers that measure microwaves.

 Zurich Instruments [Find out more](#)

# Transport in Mn spinel oxides alloyed with Zn–Ni: Polaron hopping in an inhomogeneous energy landscape

Cite as: J. Appl. Phys. **132**, 115101 (2022); doi: [10.1063/5.0105553](https://doi.org/10.1063/5.0105553)

Submitted: 24 June 2022 · Accepted: 20 August 2022 ·

Published Online: 15 September 2022



Dimitra Katerinopoulou,<sup>1,2</sup> Emmanouil Pervolarakis,<sup>3</sup> Charalampos Papakonstantinou,<sup>2,4</sup>   
Barbara Malič,<sup>5</sup> Gerwin H. Gelinck,<sup>6,7</sup> George Kiriakidis,<sup>2</sup> Zbigniew Łodziana,<sup>8</sup>   
Ioannis N. Remediakis,<sup>2,3</sup> and Eleftherios Iliopoulos<sup>1,2,a)</sup>

## AFFILIATIONS

<sup>1</sup>Department of Physics, University of Crete, P.O. Box 2208, 71003 Heraklion, Crete, Greece

<sup>2</sup>Foundation for Research and Technology Hellas (FORTH), Institute of Electronic Structure and Laser (IESL), P.O. Box 1385, 71110 Heraklion, Crete, Greece

<sup>3</sup>Department of Materials Science and Technology, University of Crete, GR-70013 Heraklion, Crete, Greece

<sup>4</sup>School of Applied Mathematical and Physical Sciences, National Technical University of Athens, Iroon Polytechniou 9, Athens 15772, Greece

<sup>5</sup>Jožef Stefan Institute, Jamova Cesta 39, 1000 Ljubljana, Slovenia

<sup>6</sup>Holst Centre/TNO, High Tech Campus 31, 5656AE Eindhoven, The Netherlands

<sup>7</sup>Department of Applied Physics, Eindhoven University of Technology, P.O. Box 513, 5600 MB Eindhoven, The Netherlands

<sup>8</sup>Institute of Nuclear Physics, Polish Academy of Sciences, Ul. Radzikowskiego 152, PL-31-342 Kraków, Poland

<sup>a)</sup>Author to whom correspondence should be addressed: [iliopoul@physics.uoc.gr](mailto:iliopoul@physics.uoc.gr)

## ABSTRACT

Electronic transport in transition metal spinel oxides is associated with small polaron hopping, either nearest-neighbor, resulting in Arrhenius activated conductivity, or variable energy, leading to a sub-Arrhenius relationship, with the conductivity logarithm being a convex function of inverse temperature. For the case of manganese spinel oxides alloyed with zinc and nickel, instances of super-Arrhenius behavior are measured, with the conductivity logarithm functional dependence on temperature deviating quadratically. Here, we study the transport in  $\text{Zn}_{0.5}\text{Ni}_x\text{Mn}_{2.5-x}\text{O}_4$  ternary oxide pellets, as a function of Ni content in the range  $0 \leq x \leq 1.25$ , in combination with structural characterization and theoretical investigations of their electronic and structural properties using density functional theory. The coexistence of cubic spinel and tetragonal Hausmannite structures is revealed along with the presence of various magnetic conformations that are metastable at room temperature. For systems where metastable structures exist, having similar formation energy but different electronic structures, conductivity is a non-trivial function of temperature. Considering nearest-neighbor polaron transfer in such an energetically inhomogeneous landscape, a new hopping mechanism model is proposed which consistently describes the temperature dependence of conductivity in this ternary alloy spinel oxide system. Understanding the underlying physical transport mechanism is vital for sensor, electrochemical, and catalytic applications.

Published under an exclusive license by AIP Publishing. <https://doi.org/10.1063/5.0105553>

## INTRODUCTION

Manganese based spinel oxides are a class of ceramic materials with a broad range of industrial interest, including sensors,<sup>1,2</sup> electrochemical energy storage and conversion,<sup>3</sup> and (photo)catalytic

applications.<sup>4</sup> Regarding temperature sensing implementations, they are used in thermistors, devices whose resistance is strongly temperature dependent. Good thermistors combine high sensitivity with fast response, reasonable sensing range, and low fabrication

cost.<sup>5</sup> The quest for good-quality devices has provided several candidate materials, such as oxides of chromium, manganese, cobalt, iron, and nickel. Among them, nickel manganese oxides,  $\text{NiMn}_2\text{O}_4$ , which have the spinel crystal structure, have recently attracted much interest.<sup>6,7</sup> They represent a class of materials with negative temperature coefficient (NTC) of resistance, superb resistivity response, robustness, and stability.

In this work, the ternary spinel system  $\text{Zn}_{0.5}\text{Ni}_x\text{Mn}_{2.5-x}\text{O}_4$  of nickel manganese oxide alloyed with zinc, an inexpensive and abundant material, is studied with the focus on their NTC properties. These alloys can crystallize in both the cubic spinel and tetragonal Hausmannite crystal structure and, for each atomic configuration, several magnetic conformations can coexist, resulting in a very rich phase space with tailored properties. They preserve the excellent thermistor properties of  $\text{NiMn}_2\text{O}_4$  and Hausmannite  $\text{Mn}_3\text{O}_4$ , while they possess very interesting electronic and magnetic properties that could be used for novel technological applications. The structural and electronic properties of  $\text{Zn}_{0.5}\text{Ni}_x\text{Mn}_{2.5-x}\text{O}_4$ , as a function of composition, were addressed theoretically by Density Functional Theory (DFT) calculations and examined experimentally by x-ray diffraction (XRD) and temperature dependent current-voltage (I-V) measurements, supplemented by electron microscopy. Identifying the relevant conduction mechanism in the temperature range of interest, as a function of composition, in the case of the ternary  $\text{Zn}_{0.5}\text{Ni}_x\text{Mn}_{2.5-x}\text{O}_4$  is of particular importance. In particular, the determination of conductivity functional relation to temperature enhances the measurement accuracy in NTC applications, while variations due to composition shed light on the underlying physical principles and guide the engineering of optimum devices. Here, it is revealed that the temperature dependence of the resistance deviates from nearest-neighbor or variable range polaron hopping behavior, in quadratic temperature terms. The experimental measurements are connected to the first-principles electronic-structure calculations and a new model for polaron hopping is obtained. This model takes into account the presence of many energy-degenerate atomic and electronic configurations.

## EXPERIMENTAL DETAILS AND THEORETICAL METHODS

The fabrication of  $\text{Zn}_{0.5}\text{Ni}_x\text{Mn}_{2.5-x}\text{O}_4$  ( $0 \leq x \leq 1.25$ ) was performed via the solid-state reaction method. Powders of  $\text{Mn}_2\text{O}_3$ ,  $\text{NiO}$ , and  $\text{ZnO}$  were weighted in appropriate proportions, mixed on a roller bench, and calcined at  $600^\circ\text{C}$  in an air oven. The resulting powders were ball-milled and mechanically pressed into pellets that were sintered at  $1250^\circ\text{C}$  overnight. Two cooling procedures were employed, one in which the sintered pellets were naturally cooled in air, while in the other were rapidly quenched.

The structural properties were studied by x-ray diffraction (XRD) using a Bruker AXS D8 Advance copper anode diffractometer (CuK $\alpha$  radiation) equipped with a nickel foil monochromator operated at 40 kV and 40 mA. The collection scan was  $2\theta$  with a range of  $10^\circ$ – $70^\circ$  and the scan rate was  $0.01^\circ$  per 10 s. Scanning Electron Microscopy (SEM) images were collected using a JEOL JSM-6390LV operating at 20 kV.

For the electrical characterization, the temperature dependent I-V characteristics of the ceramic pellets were done in a home-made oil

bath setup and were measured using a Keithley 4200 semiconductor analyzer. The temperature was ranging from room temperature (RT) up to 515 K and the applied voltage was  $\pm 1.2\text{V}$  with a back and front sweep. The structural and electronic properties of the  $\text{Zn}_{0.5}\text{Ni}_x\text{Mn}_{2.5-x}\text{O}_4$  ternary oxides were studied in the framework of Density Functional Theory (DFT) as implemented in the Vienna *ab initio* simulation package (VASP)<sup>8</sup> with the Projector Augmented Wave method (PAW).<sup>9</sup> For the exchange-correlation functional, the Generalized Gradient Approximation (GGA) was employed in the form of PBE.<sup>10</sup> In order to treat the shortcomings of DFT when dealing with materials with localized electrons, like oxides, the method of Liechtenstein *et al.*<sup>11</sup> was used as implemented in VASP.<sup>12</sup> The method introduces an explicit term to the Hamiltonian, the on-site Coulomb interaction potential “U.” The value of “U” is affected by two parameters,<sup>11</sup> U and J. The value of U, though it could change the values of the bandgaps, should not affect the trends, and, hence, in this work, a value of  $U = 4\text{eV}$  was adopted for d-electrons in all metals since it provides satisfactory results for other Mn oxides.<sup>13</sup> A value of  $J = 0\text{eV}$  was used for all atomic species. It has to be pointed out that calculated formation energies are insensitive to the choice of U parameter<sup>13,14</sup> while an increase of U results in a monotonical increase of the bandgap values, independently of nickel composition or structure (Hausmannite or spinel) considered. For oxygen atoms, a value of  $U = 0$  was employed since O d-orbitals are not involved. However, the effect of a non-zero U value for O p-orbitals was examined. As in the case of U for metal atoms, a monotonic increase in bandgap values was observed (of about 100 meV for  $U = 4\text{eV}$  and 300 meV for  $U = 12\text{eV}$ ) almost independently of nickel composition and structure. Regarding formation energy differences, between Hausmannite and spinel a very small dependence on U was observed, where even a value of  $U = 10\text{eV}$  did not change its value by more than 50 meV. All calculations were spin-polarized and allowed the atomic spins to relax. For the structures of Hausmannite and spinel, respectively, unit cells of 28 and 56 atoms were constructed, the k-point sampling was  $6 \times 6 \times 4$  and  $4 \times 4 \times 4$  and the energy-cut-off was 500 eV. The structures were allowed to relax with respect to the volume and atomic positions until all forces were below  $0.025\text{eV}/\text{\AA}$ .

## RESULTS AND DISCUSSION

### Density functional theory investigations

The spinel group compounds can be described by the general formula of  $\text{AB}_2\text{O}_4$  and most assume a cubic spinel structure with O atoms occupying the fcc lattice positions while the metals are positioned in the cavities of the oxygen lattice in tetrahedral and octahedral coordination as can be seen in Fig. 1(a) (Space Group: Fd-3m). In some cases, the atoms occupying the octahedral sites experience Jahn-Teller (J-T)<sup>15</sup> effect that causes a uniaxial elongation of the octahedra. As a result, the cubic symmetry is violated and the crystal assumes a tetragonal symmetry. This tetragonally distorted spinel structure is known as the Hausmannite structure and can be seen in Fig. 1(b) (Space Group: I41/amd).  $\text{ZnMn}_2\text{O}_4$  is notable example of the J-T effect, which is caused by the Mn ions that occupy the octahedral sites.<sup>16–18</sup>

Since these oxides can have a complex magnetic structure, like the Hausmannite  $\text{Mn}_3\text{O}_4$ ,<sup>13</sup> the spin of each atom in the computational cells was taken into account and was allowed to relax. In

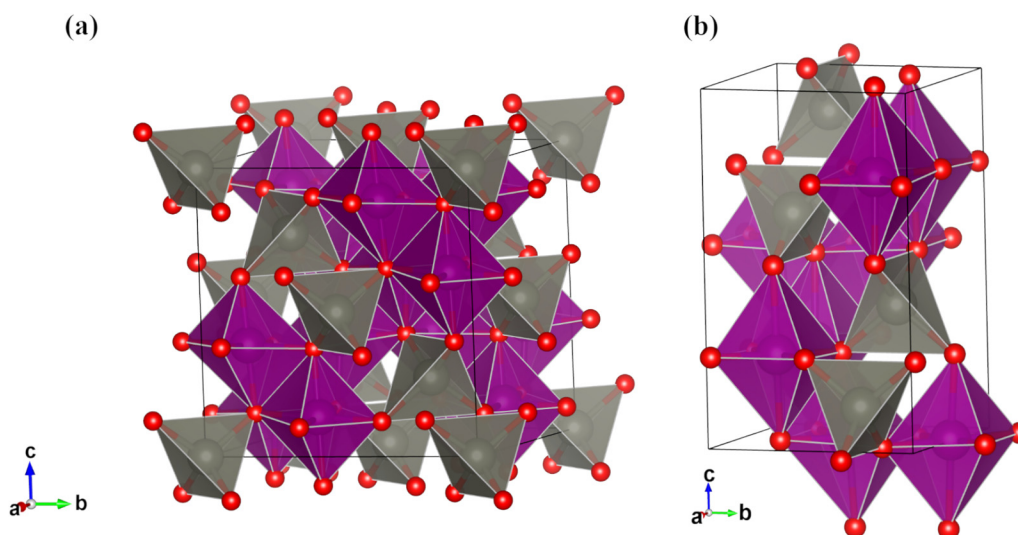


**FIG. 1.** The supercells of (a) spinel and (b) Hausmannite structures as used in the computational study. The B cation lies in the purple octahedral while the A cation in the gray tetrahedra. O atoms are represented by red spheres. The Jahn–Teller effect is responsible for the elongation of the Mn-octahedra in the c direction in (b). These structures were rendered with Vesta.<sup>19</sup>

order to investigate site preference for the atoms, we consider several different initial configurations for the calculations, which are then fully relaxed in terms of lattice constants and atomic coordinates. For each structure, several different magnetic configurations are considered. In total, we simulate more than 200 structures with DFT.

Both the spinel and Hausmannite structures of these materials were considered (Fig. 1). Due to the number of different metallic species, the two types of sites they can occupy, and the spin degree

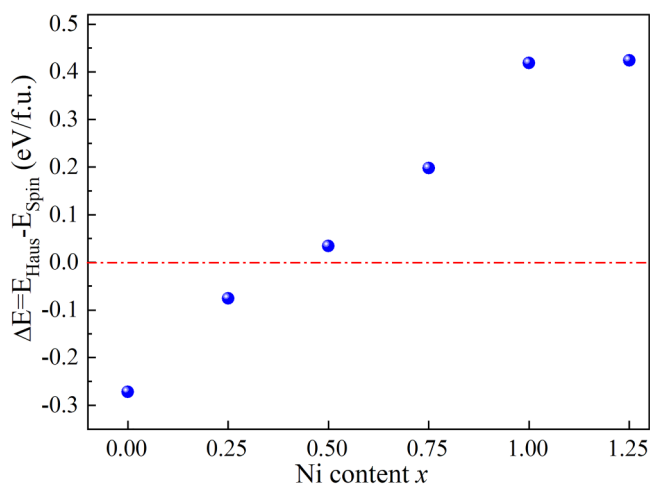


**FIG. 2.** Difference in formation energy of the most stable Hausmannite and spinel structures of  $\text{Zn}_{0.5}\text{Ni}_x\text{Mn}_{2.5-x}\text{O}_4$  as calculated from DFT + U.

of freedom, the possible configuration space is really vast. This makes the exploration of all the possible configurations in both structures extremely difficult. Initial guesses were made based on similar materials like the Hausmannite  $\text{ZnMn}_2\text{O}_4$ <sup>20</sup> in which Zn has tetrahedral and Mn octahedral coordination or like  $\text{NiMn}_2\text{O}_4$ ,<sup>20</sup> an inverse spinel with Ni atoms at half octahedral sites and Mn occupying the tetrahedral and the other half octahedral sites. From the configurations that were tested, similarly to the initial guesses, Mn atoms can occupy both tetrahedral and octahedral sites, like in the case of  $\text{Zn}_{0.5}\text{Mn}_{2.5}\text{O}_4$ , while the Zn atoms show a strong preference of the tetrahedral site. The site preference of Ni is more complicated since it is structure and concentration dependent, preferring tetrahedral sites in the Hausmannite, by about 50 meV per formula unit (f.u.) per Ni atom, and octahedral sites in the spinel (by about 100 meV/f.u./Ni). Octahedrally coordinated Ni does not cause the J–T distortion, favoring the cubic structure. On the other hand, if Ni is positioned at the tetrahedral sites, the J–T effect from the octahedral Mn persists, making the spinel less energetically favored. However, there are a few exceptions to this general preference of Ni. For example, spinel  $\text{Zn}_{0.5}\text{Ni}_{1.25}\text{Mn}_{1.25}\text{O}_4$ , where, after filling half the octahedral sites the extra Ni atoms prefer to replace tetrahedral instead of octahedral Mn (by about 100 meV/f.u./Ni), implying that replacing more than half of the octahedral Mn is unfavorable. Additionally, in the case of the Hausmannite structure, for Ni concentrations equal to or higher than  $x = 0.75$ , all the tetrahedral sites are occupied by Zn and Ni atoms; thus, the extra Ni had to occupy octahedral sites. As a result of these considerations, the lowest energy structure of the alloy is Hausmannite when Ni concentration is lower than 50% and spinel for all higher concentrations. The energy difference between the spinel and Hausmannite structures increases almost

linearly with Ni concentration until  $x=1.00$ . For  $x=1.25$ , the numbers of Ni and Mn atoms are equal, and no further increase of the energy gain of the spinel structure is found. The calculated energy difference between the most stable Hausmannite and spinel structures for the whole range of  $x$  studied is presented in Fig. 2.

The DFT+U results imply a clear preference of the Hausmannite structure in the absence of Ni atoms while the spinel structure is strongly favored for the two highest Ni concentrations. For materials with intermediate Ni content, the two structures have similar energies, suggesting a possible coexistence of both phases. The lattice parameters of the most stable materials for both structures are presented in Table I, in excellent agreement with the experimental values discussed below.

The ground state investigation revealed that the magnetic configuration of these materials is of primary importance. In the cubic spinel, the ground state magnetization in most cases involved the Mn atoms having parallel spins and antiparallel with the Ni atoms. Element and orbital decomposed spin-polarized density of states (DOS) plots for Hausmannite and spinel  $Zn_{0.5}Mn_{2.5}O_4$  cases, respectively, are shown in Figs. S1 and S2 in the supplementary material, while Fig. S3 in the supplementary material presents an example of spin-polarized DOS plots for the Ni content  $x=1.00$  spinel case. In the case of Hausmannite, a ferrimagnetic configuration was the most stable one with half the octahedral atoms being parallel to the tetrahedral and antiparallel to the rest octahedral ones. In all cases, the Zn atoms are at second oxidation state and, thus, do not contribute to the magnetization, relaxing to zero atomic magnetic moments.

The phase space of the magnetic configurations was further explored by flipping the spin of selected atoms of the most stable structures and relaxing the atomic positions. Several magnetic configurations were found with energies no more than 25 meV/f.u.

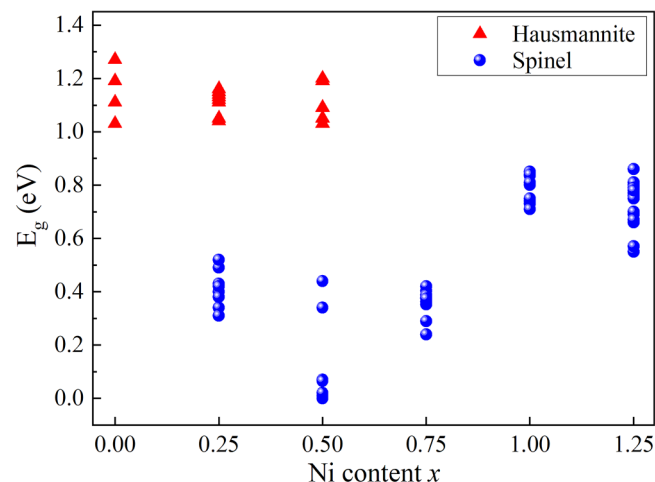


**FIG. 3.** The calculated bandgaps of the most stable structures and their magnetic polytypes that are apart in energy at most by  $1k_B T$  at room temperature (25 meV/f.u.). The bandgaps were obtained from Density of States (DOS) calculations in which the  $k$ -point sampling was increased to  $12 \times 12 \times 8$  and  $8 \times 8 \times 8$  for Hausmannite and spinel, respectively.

apart from the most stable ones, with the change in magnetic configuration being often accompanied by a change of the electronic bandgap of the materials (see Table SI and example in Fig. S4 in the supplementary material). The range of bandgaps for the most stable structures is introduced in Fig. 3.

### Structural properties

Structural analysis of the synthesized materials was carried out by XRD, with the obtained diffraction patterns presented in Fig. 4. For the sample without Ni ( $x=0$ ), a pure tetragonal phase is revealed, while with increasing Ni content, the cubic phase is promoted, transitioning to a mix of cubic and tetragonal phases and then to pure cubic phases. For  $x=0.25$  and  $0.50$ , a coexistence of the phases is present with the tetragonal phase being more pronounced, then at  $x=0.75$  a mixed phase with the cubic more pronounced, and, finally, for  $x=1.00$  and  $1.25$ , pure cubic phases are observed. Thus, the structures obtained by the XRD data of the air-cooled samples are in excellent agreement with the theoretical calculations. The composition dependence of prevailing structures and the presence of mixed phases accurately reflect the formation energy differences predicted between the spinel and Hausmannite structures. In the case of quenched materials, XRD patterns show mixed phases in all concentrations, even at the extremes of  $x=0.25$  and  $1.25$ . Such increased intermixing is expected due to trapping by fast cooling of the less energetically favorable phases existing at the high sintering temperatures. The lattice parameters extracted from the XRD spectra, presented in Table I, agree with the theoretically predicted ones, deviating at most by 5%, that is, within typical accuracy for DFT + U calculations.

The morphology of the ceramic pellets was investigated with Scanning Electron Microscopy (SEM). The images obtained from the surface of pellets, for  $3000\times$  magnification, reveal good crystallinity without any signs of porosity (Fig. S5 in the supplementary material).

### Electrical properties characterization

The electrical conductivity of the ceramic pellets was characterized by temperature dependent (300–515 K range) current–voltage (I–V) measurements. Typically, forward–backward scanned I–V curves were linear, without indication of hysteresis, in all cases except for the Ni-free air-cooled pellets where a minimal hysteresis was observed at low temperatures ( $\leq 320$  K), thus excluding self-heating effects in the I–V measurements. An example of temperature dependent I–V measurements is depicted in Fig. 5(a) that corresponds to an air-cooled pellet with Ni content  $x=1.00$ . The I–V characteristics were also fully reproducible and no resistance hysteresis was observed upon heating and cooling cycling. The absence of such hysteretic phenomena excludes the possibility of sample’s structural transformation upon heating, a phenomenon observed sometimes in spinel oxides.<sup>21,22</sup> To a first approximation, the resistance dependence on temperature follows an inverse Arrhenius relation,<sup>3</sup>

$$R(T) = R_0 \exp\left(\frac{E_a}{k_B T}\right), \quad (1)$$

where  $R_0$  is the specific resistance,  $E_a$  is the activation energy for

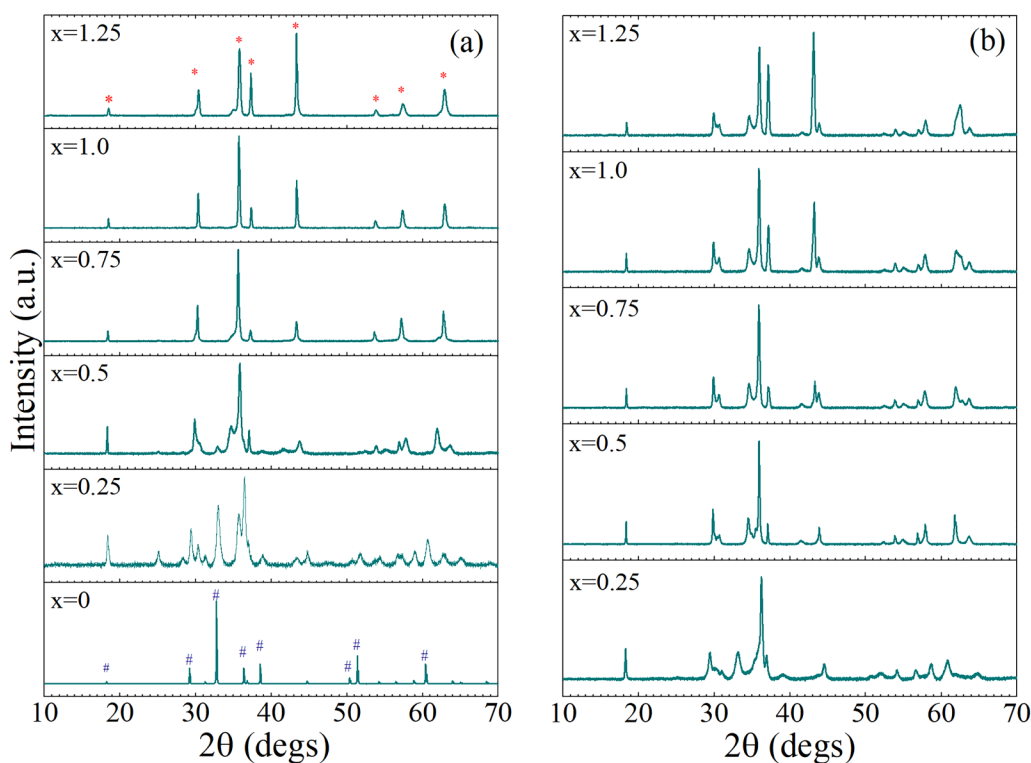


FIG. 4. XRD patterns of  $\text{Zn}_{0.5}\text{Ni}_x\text{Mn}_{2.5-x}\text{O}_4$  of (a) air-cooled and (b) quenched pellets.

conductivity, and  $k_B$  is the Boltzmann constant. The pre-exponential factor  $R_0$  is considered temperature independent, in this approximation, since any possible temperature dependence is slower than the one of the exponential part. Its physical significance depends on the transport mechanism involved and the density-of-states characteristics near the Fermi-energy. As is apparent from Eq. (1), the resistance exponentially decreases with increasing temperature, which is a typical characteristic of Negative Temperature Coefficient (NTC) thermistors. An example Arrhenius plot for the data of  $x = 1.0$  is depicted in Fig. 5(a), where an apparent drop in the sample resistance of about three decades is observed between temperature change from

300 to 515 K. A summary of the temperature dependent electrical characteristics for all cases is presented in Figs. 5(b) and 5(c), where the corresponding values of the exponential pre-factor  $R_0$  and the activation energy  $E_a$  are plotted. The latter are extracted from the slope of natural logarithm of resistance as a function of the reciprocal absolute temperature. Another parameter widely used in the industry for identifying possible NTC candidates is the thermal constant  $B$ ,<sup>23</sup> which is directly related to  $E_a$  ( $B = \frac{E_a}{k_B}$ ),<sup>7</sup> and is also presented in Fig. 5(c). Both air-cooled and quenched series follow the same trend with regard to their Ni content, with  $E_a$  exhibiting a swift decrease at

TABLE I. Lattice parameters as calculated from the XRD patterns (experimental) and DFT + U calculations (theoretical).

$\text{Zn}_{0.5}\text{Ni}_x\text{Mn}_{2.5-x}\text{O}_4$	Experimental		Theoretical	
	Hausmannite a = b, c (Å)	Spinel a = b = c (Å)	Hausmannite a = b, c (Å)	Spinel a = b = c (Å)
x = 0	5.723, 9.317	...	5.799, 9.597	8.614
x = 0.25	5.722, 9.389	8.346	5.774, 9.555	8.565
x = 0.50	5.733, 9.284	8.386	5.764, 9.539	8.511
x = 0.75	...	8.356	5.741, 9.502	8.468
x = 1.00	...	8.334	5.721, 9.469	8.427
x = 1.25	...	8.331	5.699, 9.432	8.394

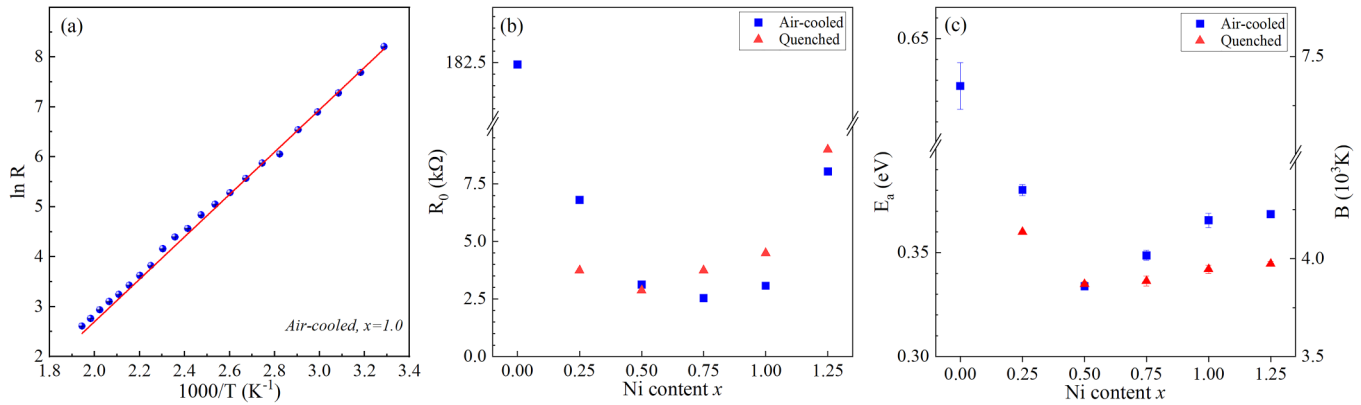


**FIG. 5.** Thermoelectric behavior of the ceramic materials. (a) Arrhenius plot of resistance vs temperature for the case air-cooled pellet with Ni content  $x = 1.0$ . (b) The pre-exponential factor  $R_0$  and (c) the determined activation energies for all cases. Note the y axis breaks in (b) and (c).

lower values of  $x$  ( $x \leq 0.5$ ) while gradually increasing for higher Ni contents. Note that the Ni-free case displayed a significantly higher resistance performance, as observed by the much higher  $R_0$  value and an increased drop rate upon heating. This U-functional dependence of  $R_0$  and  $E_a$  values correlates with the similar dependence, as derived by DFT calculations, of the spinel's phase bandgaps on Ni content  $x$ , which will be discussed in detail below.

### Conductivity transport mechanism

A mono-exponential Arrhenius relation of the resistivity's dependence on temperature is a useful engineering approximation to derive a figure-of-merit parameter of the performance of relative materials in NTC applications; however, it does not accurately reflect the true relationship in all cases. The functional behavior of conductivity on temperature is directly related to the underlying transport mechanism. In polarizable dielectric oxide crystals, the free electrons (or holes) with large effective mass interact with neighbor ionic species, causing local lattice distortions.<sup>24</sup> The coupling of the charged carriers with lattice vibrations (phonons) leads to the formation of self-localized<sup>25</sup> fermionic quasiparticles known as polarons.<sup>26–30</sup> In spinel manganese compounds, charge transport is associated with a small polaron<sup>31</sup> hopping mechanism between localized polaron states.<sup>32</sup> Thus, such materials can be classified as Coulomb glasses.<sup>33</sup> The conductivity is dictated by charged carrier jumps due to polaron-phonon interactions<sup>34</sup> and is approximated as a percolation process in a random resistor network,<sup>35</sup> similar to the case of low impurity semiconductors at low temperatures. The specific characteristics of the conduction are dependent on the competing strengths, relative to the average phonon energy, of the spatial and energy separation terms contributing to the percolation threshold and the density of states (DOS) distribution near the Fermi energy.<sup>36</sup> Thus, the resistance dependence on temperature assumes, in general, a functional relation of the form

$$R(T) = R_0 T^a \exp\left(\frac{T_0}{T}\right)^p, \quad (2)$$

where the values of the exponents  $a$ ,  $p$  and parameter  $T_0$  depends on the particular aspects of the hopping process. In the lower temperature regime, given a constant DOS, Mott variable range hopping (VRH) model predicts a  $p = \frac{1}{4}$ , while in the case of a vanishing DOS at the Fermi level, due to the Coulomb gap, Efros and Shklovskii<sup>37</sup> calculated the exponents  $a = 2p$  and  $p = (n+1)/(n+4)$  for a DOS energy functional dependence  $g(\epsilon) \sim |\epsilon - E_F|^n$ . In the case of the non-adiabatic limit at higher temperatures, where the importance of spatial separation of hopping sites dominates, the nearest-neighbor hopping (NNH) model is mostly applicable<sup>33,34</sup> and the temperature dependence of resistance tends to an inverse Arrhenius one with the corresponding exponent values  $a = p = 1$ ,

$$R_{NN}(T) = R_{NN,0} k_B T \exp\left(\frac{T_0}{T}\right). \quad (3)$$

It should be pointed out that in the case of higher order spinel oxide alloys,<sup>38</sup> the simple small polaron transport models may be inadequate to fully describe the conduction mechanism, due to asymmetric hopping barriers between octahedral sites occupied by different ionic species.

To determine the values of the characteristic exponent  $p$  in Eq. (2), the methodology of Efros and Shklovskii<sup>36</sup> was applied, by calculating the dimensionless activation energy  $W$ , from the resistance vs temperature  $R(T)$  data,

$$W(T) = T^{-1} \frac{d(\ln R)}{d(T^{-1})} \quad (4)$$

and retrieving the  $p$  values by linear regression to the  $-\ln W$  vs  $\ln T$  plots, for each dataset. An example of this analysis is depicted in the data of Fig. 6(a) for the case of the air-cooled sample with Ni content equal to  $x = 0.75$ , while in Fig. 6(b), the resulting exponent  $p$  values for all cases are summarized. As observed in the data of Fig. 6(b), a conductivity mechanism consistent with the non-adiabatic limit NNH model of Eq. (3) is followed for the cases of low ( $x \leq 0.25$ ) and high ( $x > 1$ ) nickel content, since in these cases

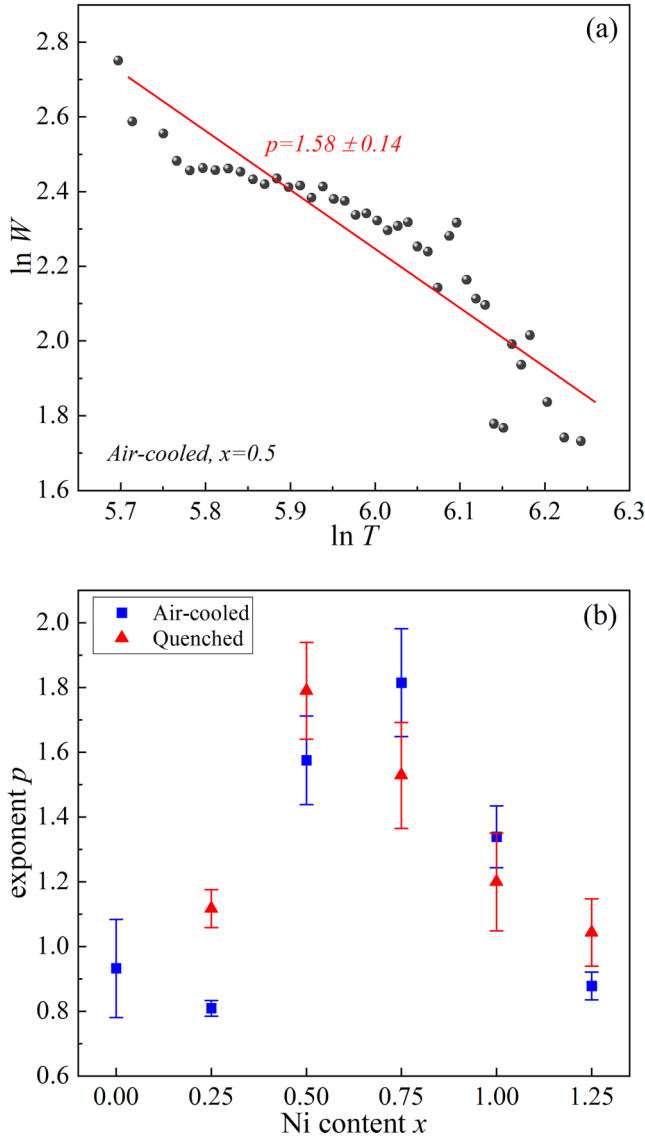


**FIG. 6.** (a) Example of  $\ln(W)$  vs  $\ln(T)$  for the case of air-cooled sample with Ni content  $x = 0.5$  and (b) collective plot of  $p$  exponent values vs Ni content  $x$  for air-cooled and quenched sample series. It has to be pointed out that the scattering of data points in (a) is typical and relates to the derivative  $d(\ln R)/dT^{-1}$  involved. This scattering is reflected in the error bars of the  $p$  exponent values.

$p \approx 1$  (an example is given in Fig. S6 in the [supplementary material](#)). Such a NNH type conduction is consistent with the elevated temperature measurement range investigated. However, in the intermediate nickel composition cases, the temperature scaling exponent  $p$  exceeds unity, thus excluding simple VRH or NNH mechanisms association with the underlying physical processes. Instead, a super-Arrhenius behavior is observed, a function of the form  $\exp[-(\frac{\epsilon}{T})^p]$  with  $p > 1$ . In extreme cases, it approaches a

quadratic dependence of the logarithm of conductance on inverse temperature, a fact that is also confirmed by direct fitting of the  $R(T)$  data. Interestingly, similar temperature dependences have been observed for the electrical conductivity in a number of ionic glass systems.<sup>39–41</sup>

The physical processes involved in the electrical conductivity of this spinel ternary alloy oxide system can be elucidated by considering correlations between (a) the experimentally derived values of the conductance activation energies  $E_a$  of Fig. 5(c) and the scaling exponents  $p$  of Fig. 6(b), the theoretically calculated ranges of possible energy bandgap values  $E_g$ , for the most stable lattice and spin configurations, depicted in Fig. 3. The pre-exponential factor  $R_0$  values [Fig. 5(b)] follow the calculated spinel bandgaps trend, pointing to the fact that the spinel phase component is the dominant one, concerning the conductivity properties, as expected due to the lower corresponding bandgap values. This is particularly highlighted in the case of Ni-free specimen where a pure Hausmannite phase is theoretically predicted and confirmed by XRD and whose resistivity is much higher compared to the nickel containing cases. Furthermore, an important relationship between the two characteristic measures depicted in Figs. 4 and 6(b) is observed. In the case of compositions where stable configurations lead to closely spaced spinel energy gaps (narrow distribution of  $E_g$ ), the electrical conductivity tends to follow an Arrhenius temperature dependence, compliant with a classical NNH mechanism. In contrast, in cases where the  $E_g$  value distribution of near-stable polytypes is broader and the mean of the distribution is lower, the  $p$  exponent value increases and the conductivity behavior deviates to a super-Arrhenius relationship. In the latter case, the conductivity process relates to percolation by hopping in a complex, largely inhomogeneous energy landscape, where the distribution of nearest neighbors' energy differences is broad. To examine conduction by small polarons transfers between neighboring sites in such case, called herein variable-energy nearest-neighbor-hopping (VE-NNH), a gaussian distribution of sites' energy with mean value  $\epsilon_0$  (referenced to the system quasi-constant Fermi level) and with standard deviation  $\sigma$  is assumed,

$$g(\epsilon) = \frac{1}{\sigma\sqrt{2\pi}} \exp\left(-\frac{(\epsilon - \epsilon_0)^2}{2\sigma^2}\right). \quad (5)$$

Then, the mean time needed for a polaron with energy  $\epsilon_i$  to transfer to an unoccupied site with energy  $\epsilon_i + \Delta\epsilon$ , due to interaction with phonons, is given by

$$\tau(\epsilon_i) \propto \frac{1}{\sigma\sqrt{2\pi}} \int_{-\infty}^{+\infty} d\Delta\epsilon e^{\beta\Delta\epsilon} e^{-\frac{(\epsilon_i - \epsilon_0 + \Delta\epsilon)^2}{2\sigma^2}} \left(1 - e^{-\beta(\epsilon_i - \epsilon_0 + \Delta\epsilon)}\right), \quad (6)$$

where  $\beta = 1/k_B T$  and the approximation of polaron sites' occupation by Boltzmann's distribution is justified, assuming  $\beta\epsilon_0 \gg 1$ , by the presence of the gaussian term in the integrand.

Then, the resistivity  $\rho(T)$  using again the Boltzmann approximation for sites' occupation probability can be evaluated as

$$\rho^{-1}(T) = \rho_0^{-1} \frac{1}{\sigma\sqrt{2\pi}} \int_{-\infty}^{+\infty} d\epsilon e^{\frac{(\epsilon - \epsilon_0)^2}{2\sigma^2}} e^{-\beta\epsilon} \frac{1}{\tau(\epsilon)}, \quad (7)$$



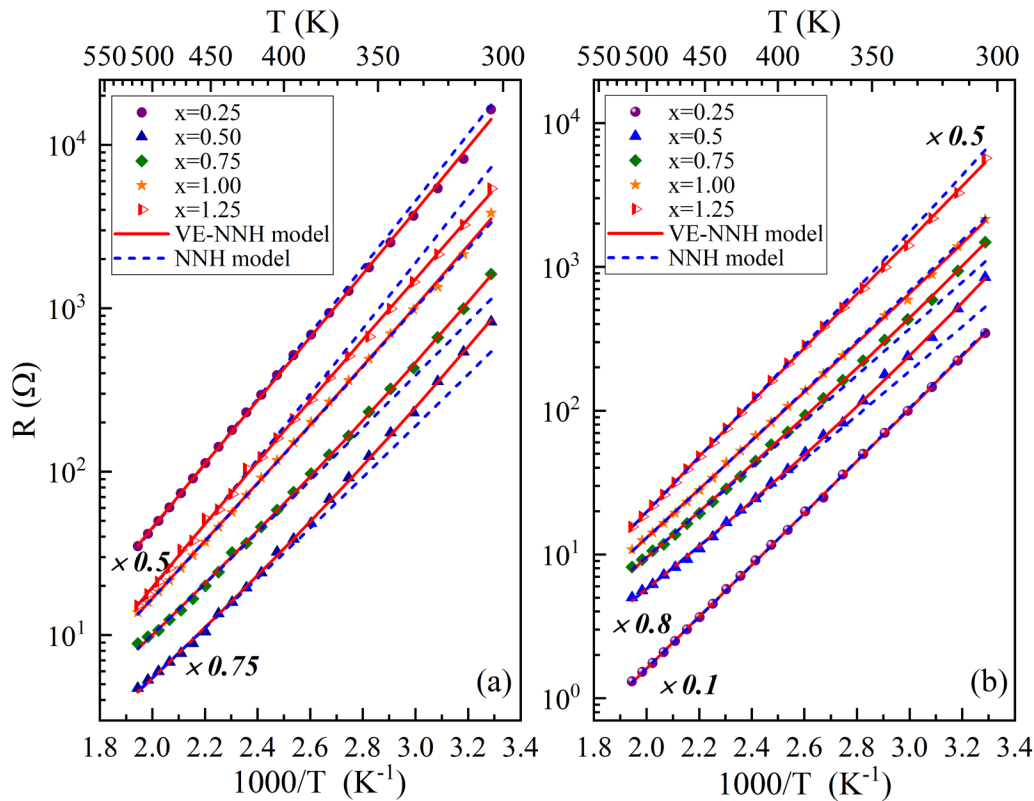


**FIG. 7.** Plots of resistance vs inverse temperature for the case of (a) air-cooled and (b) quenched samples and the corresponding fitted curves for the case of VE-NNH (solid red lines) and NNH (dotted blue lines) transport mechanisms. Some data series and the corresponding curves were translated vertically (by a multiplication factor indicated) for reasons of clarity.

which leads to the functional dependence of the resistance on temperature,

$$R_{VE-NN}(T) = R_0 e^{\frac{T_0}{T}} \left( e^{\frac{\delta^2}{T^2}} - 1 \right), \quad (8)$$

where the scaled parameters  $T_0 = \epsilon_0/k_B$  and  $\delta = \sigma/\sqrt{2}k_B$  relate to the mean position and the broadening of the energy gaussian distribution of polaron states. In the case that a very narrow distribution

is considered,  $g(\epsilon) \rightarrow \delta(\epsilon - \epsilon_0)$ , the usual NNH relation of Eq. (3) is retrieved. It should also be pointed out that Eq. (8) should rather be considered as a phenomenological model, given the approximate nature of the hopping transport analysis and the assumptions used. In a more rigorous treatment, more complex dependencies of the parameters  $T_0$  and  $\delta$  on the parameters of sites' energy distribution as well as for the overall temperature functional form is expected.

In view of the above, the temperature dependence of resistance of the  $Zn_{0.5}Ni_xMn_{2.5-x}O_4$  ternary oxides, as a function of Ni

**TABLE II.** Fitted values of the parameters  $T_0$  and  $\delta$  for the VE-NNH model.

$Zn_{0.5}Ni_xMn_{2.5-x}O_4$	Air-cooled		Quenched	
	$T_0$ (K)	$\delta$ (K)	$T_0$ (K)	$\delta$ (K)
x = 0.25	$3120 \pm 220$	$425 \pm 73$	$2640 \pm 88$	$476 \pm 24$
x = 0.50	$1330 \pm 200$	$684 \pm 31$	$1040 \pm 210$	$718 \pm 30$
x = 0.75	$1470 \pm 180$	$664 \pm 30$	$1700 \pm 150$	$618 \pm 27$
x = 1.00	$2390 \pm 170$	$532 \pm 38$	$2350 \pm 150$	$495 \pm 38$
x = 1.25	$3310 \pm 220$	$290 \pm 120$	$3150 \pm 150$	$372 \pm 57$

content, is examined in the context of the small polaron VE-NNH transport mechanism. The resistance vs inverse absolute temperature for the air-cooled and quenched sample series is shown in Fig. 7 for all Ni contents higher than zero. The data are fitted using both NNH (blue dotted lines) and VE-NNH (red lines) transport models, corresponding to Eqs. (3) and (8), respectively. In the case of NNH fits, the upper half temperature data range was used for consistency with the non-adiabatic limit. Significant differences between the two models are observed, with the VE-NNH model consistently describing the temperature dependence of resistance in the entire range, including the lower one, where quadratic deviations from the NNH model are observed. This is particularly emphasized in the case of intermediate compositions where DFT calculations predict a broader distribution of possible bandgaps between different magnetic conformations and lower overall bandgap values for the dominating spinel phase. The obtained values of the parameters  $T_0$  and  $\delta$  for the VE-NNH model fits are presented in Table II. The values and their dependence on Ni composition are in agreement with the DFT calculations, thus emphasizing the underlying physical mechanism leading to the variable-energy nearest-neighbor hopping type of transport mechanism, namely, the reduction of and the coexistence of a wide distribution of bandgaps due to the presence of metastable spinel magnetic polytypes.

## CONCLUSIONS

The electronic transport properties of  $\text{Zn}_{0.5}\text{Ni}_x\text{Mn}_{2.5-x}\text{O}_4$  ternary oxides, with varying Ni concentrations  $0 \leq x \leq 1.25$ , are studied by temperature dependent I–V measurements in the range of 300–515 K and their structure by x-ray diffraction. A super-Arrhenius activation of conductivity is revealed, with the presence of a quadratic temperature functional term, which is more pronounced in mid-composition cases. First principle DFT + U calculations show that the tetragonal Hausmannite crystal structure is favored in the absence of nickel, but the formation energy difference between Hausmannite and cubic spinel structure decreases monotonically with increasing Ni concentration, with the spinel phase becoming the dominant one for  $x \geq 0.75$ , in close agreement with XRD measurements. The spinel phase exhibits reduced energy bandgaps with a parabolic dependence on composition and a minimum at  $x = 0.5$ . Furthermore, a variety of atomic spin configurations with small formation energy differences, in the range of 25 meV, but different bandgaps are predicted, leading to an inhomogeneous energy landscape. Considering small polaron transport by nearest-neighbor hopping in such an environment, approximated by a gaussian distribution of sites' energetic positions, leads to a new “variable-energy nearest-neighbor hopping” model for the resistance functional dependence on temperature, which elucidates the origin of super-Arrhenius conductivity activation and consistently describes the experimental data.

## SUPPLEMENTARY MATERIAL

See the [supplementary material](#) for examples of spin decomposed, elemental, and orbital density of states plots for ranges of total and individual atoms calculated magnetizations, scanning electron microscopy images of the samples' surface, and examples of electrical data characteristic of quenched series samples.

## ACKNOWLEDGMENTS

This research is co-financed by the Greece and the European Union (European Social Fund-ESF) through the Operational Programme “Human Resources Development, Education and Lifelong Learning 2014-2020” in the context of the project “MnNiO<sub>x</sub>:Zn CERAMIC ALLOYS FOR HIGH PRECISION TEMPERATURE SENSORS” (MIS 5050587). The authors gratefully acknowledge Professor Pim Groen from the Delft University of Technology for providing materials and inspiration. I.N.R. and E.P. acknowledge CPU time in the National HPC facility. Z.Ł. acknowledges CPU allocation at PL-Grid infrastructure.

## AUTHOR DECLARATIONS

### Conflict of Interest

The authors have no conflicts to disclose.

### Author Contributions

D.K. and E.P. contributed equally to this work

**Dimitra Katerinopoulou:** Formal analysis (equal); Visualization (equal); Writing – original draft (equal). **Emmanouil Pervolarakis:** Formal analysis (equal); Visualization (equal); Writing – original draft (equal). **Charalampos Papakonstantinopoulos:** Formal analysis (supporting). **Barbara Mali:** Resources (supporting). **Gerwin H. Gelinck:** Resources (lead). **George Kiriakidis:** Resources (supporting). **Zbigniew Łodziana:** Formal analysis (equal); Methodology (equal); Validation (equal); Writing – original draft (equal). **Ioannis N. Remediakis:** Formal analysis (equal); Methodology (equal); Validation (equal); Writing – original draft (equal). **Eleftherios Iliopoulos:** Conceptualization (lead); Formal analysis (equal); Methodology (equal); Supervision (lead); Writing – original draft (equal).

## DATA AVAILABILITY

The data that support the findings of this study are available from the corresponding author upon reasonable request.

## REFERENCES

- <sup>1</sup>A. Feteira, *J. Am. Ceram. Soc.* **92**, 967–983 (2009).
- <sup>2</sup>W. B. S. Machini, C. S. Martin, M. T. Martinez, S. R. Teixeira, H. M. Gomes, and M. F. S. Teixeira, *Sens. Actuators B: Chem.* **181**, 674 (2013).
- <sup>3</sup>K. Zhang, X. Han, Z. Hu, X. Zhang, Z. Tao, and J. Chen, *Chem. Soc. Rev.* **44**, 699–728 (2015).
- <sup>4</sup>T. Tatarchuk, B. Al-Najar, M. Bououdina, and M. A. Aal Ahmed, *Handbook of Ecomaterials* (Springer, Cham, 2018), pp. 1701–1750.
- <sup>5</sup>O. S. Aleksic and P. M. Nikolic, *Facta Univ. Ser.: Electron. Energ.* **30**, 267–284 (2017).
- <sup>6</sup>K. Park and D. Y. Bang, *J. Mater. Sci.: Mater. Electron.* **14**, 81–87 (2003).
- <sup>7</sup>D. Katerinopoulou, P. Zalar, J. Sweelssen, G. Kiriakidis, C. Rentrop, P. Groen, G. H. Gelinck, J. van den Brand, and E. C. P. Smits, *Adv. Electron. Mater.* **5**, 1800605 (2019).
- <sup>8</sup>G. Kresse and J. Furthmüller, *Phys. Rev. B* **54**(16), 169 (1996).
- <sup>9</sup>G. Kresse and D. Joubert, *Phys. Rev. B* **59**, 1758–1775 (1999).
- <sup>10</sup>J. P. Perdew, K. Burke, and M. Ernzerhof, *Phys. Rev. Lett.* **77**, 3865–3868 (1996).

- <sup>11</sup>A. I. Liechtenstein, V. I. Anisimov, and J. Zaanen, *Phys. Rev. B* **52**, R5467–R5470 (1995).
- <sup>12</sup>A. Rohrbach, J. Hafner, and G. Kresse, *J. Phys.: Condens. Matter* **15**, 979–996 (2003).
- <sup>13</sup>C. Franchini, R. Podloucky, J. Paier, M. Marsman, and G. Kresse, *Phys. Rev. B* **75**, 195128 (2007).
- <sup>14</sup>C. Loschen, J. Carrasco, K. M. Neyman, and F. Illas, *Phys. Rev. B* **75**, 1 (2007).
- <sup>15</sup>Y.-K. Sun, Y. S. Jeon, and H. J. Lee, *Electrochem. Solid-State Lett.* **3**, 7 (1999).
- <sup>16</sup>S. Asbrink, A. Waškowska, L. Gerward, J. S. Olsen, and E. Talik, *Phys. Rev. B* **60**, 12651–12656 (1999).
- <sup>17</sup>S. C. Tarantino, M. Giannini, M. A. Carpenter, and M. Zema, *IUCr* **3**, 354–366 (2016).
- <sup>18</sup>P. Patra, I. Naik, H. Bhatt, and S. D. Kaushik, *Phys. B: Condens. Matter* **572**, 199–202 (2019).
- <sup>19</sup>K. Momma and F. Izumi, *J. Appl. Crystallogr.* **44**, 1272–1276 (2011).
- <sup>20</sup>R. W. G. Wyckoff, *Crystal Structures* (Interscience Publishers, 1964).
- <sup>21</sup>B. Talic, P. V. Hendriksen, K. Wiik, and H. L. Lein, *Solid State Ion.* **326**, 90–99 (2018).
- <sup>22</sup>C. B. Azzoni, M. C. Mozzati, A. Paleari, M. Bini, D. Capsoni, G. Chiodelli, and V. Massarotti, *Z. Naturforsch. A* **54**, 579–584 (1999).
- <sup>23</sup>C. Metzmacher, W. A. Groen, and I. M. Reaney, *Phys. Status Solidi (A)* **181**, 369–386 (2000).
- <sup>24</sup>L. D. Landau, *Phys. Z. Sowjetunion* **3**, 644–645 (1933).
- <sup>25</sup>S. I. Pekar, *Zh. Eksp. Teor. Fiz* **16**, 341 (1946).
- <sup>26</sup>S. T. Kshirsagar and C. D. Sabane, *Jpn. J. Appl. Phys.* **10**, 794–802 (1971).
- <sup>27</sup>B. Gillot, R. Legros, R. Metz, and A. Rousset, *Solid State Ion.* **51**, 7–9 (1992).
- <sup>28</sup>R. Metz, *J. Mater. Sci.* **35**, 4705–4711 (2000).
- <sup>29</sup>R. Schmidt, A. Basu, and A. W. Brinkman, *Phys. Rev. B* **72**, 115101 (2005).
- <sup>30</sup>H. Han, J. S. Lee, J. H. Ryu, K. M. Kim, J. L. Jones, J. Lim, S. Guillemet-Fritsch, H. C. Lee, and S. Mhin, *J. Phys. Chem. C* **120**, 13667–13674 (2016).
- <sup>31</sup>T. Holstein, *Ann. Phys.* **8**, 343–389 (1959).
- <sup>32</sup>C. Franchini, M. Reticcioli, M. Setvin, and U. Diebold, *Nat. Rev. Mater.* **6**, 756 (2021).
- <sup>33</sup>N. F. Mott and E. A. Davis, *Electronic Processes in Non-Crystalline Materials*, 2nd ed. (Oxford University Press, Oxford, 1993).
- <sup>34</sup>J. Schnakenberg, *Phys. Status Solidi (B)* **28**, 623–633 (1968).
- <sup>35</sup>A. Miller and E. Abrahams, *Phys. Rev.* **120**, 745–755 (1960).
- <sup>36</sup>B. I. Shklovskii and A. L. Efros, *Electronic Properties of Doped Semiconductors*, 1st ed. (Springer-Verlag, Berlin, 1984).
- <sup>37</sup>A. L. Efros and B. I. Shklovskii, *J. Phys. C: Solid State Phys.* **8**, L49–L51 (1975).
- <sup>38</sup>A. Bhargava, R. Eppstein, J. Sun, M. A. Smeaton, H. Paik, L. F. Kourkoutis, D. G. Schlom, M. C. Toroker, and R. D. Robinson, *Adv. Mater.* **32**, 2004490 (2020).
- <sup>39</sup>J. Kincs and S. W. Martin, *Phys. Rev. Lett.* **76**, 70–73 (1996).
- <sup>40</sup>S. Murugavel, *Phys. Rev. B* **72**, 134204 (2005).
- <sup>41</sup>Y. Okada, M. Ikeda, and M. Aniya, *Solid State Ion.* **281**, 43–48 (2015).